The role of resonance and bandgaps in high k^2_{eff} transducers

Christopher J. Sarabalis,* Yanni D. Dahmani, Agnetta Y. Cleland, and Amir H. Safavi-Naeini†
Department of Applied Physics and Ginzton Laboratory, Stanford University
348 Via Pueblo Mall, Stanford, California 94305, USA
(Dated: January 21, 2022)

Bandgaps formed in a piezoelectric transducer with large coupling, k^2_{eff}, qualitatively modify its electrical response. This regime in which electrical loading strongly couples forward and backward waves occurs in thin-film lithium niobate which has recently become available and amenable to nanopatterning. In this work, we study how resonance and bandgaps modify the design and performance of transducers and delay lines in thin-film lithium niobate. These films are an attractive platform for GHz frequency applications in low-power RF analog signal processing, optomechanics, and quantum devices due to their high coupling, low loss, excellent optical properties, and compatibility with superconducting quantum circuits. We demonstrate aluminum IDTs in this platform for horizontal shear (SH) waves between 1.2 and 3.3 GHz and longitudinal waves between 2.1 and 5.4 GHz. For the SH waves, we measure a piezoelectric coupling coefficient of 13% and 6.0 dB/mm propagation losses in delay lines up to 1.2 mm with a 300 ns delay in air at room temperature. Reflections from electrical loading when k^2_{eff} is large lead to a departure from the impulse response model widely used to model surface acoustic wave devices. Finite element method models and an experimental finger-pair sweep are used to characterize the role of resonance in these transducers, illuminating the physics behind the anomalously large motional admittances of these small-footprint IDTs.

I. INTRODUCTION

Piezoelectric devices enjoy a wide range of modern applications in microwave, optical, and quantum systems thanks to the development of low-loss piezoelectric materials with large piezoelectric coupling such as lithium niobate [1]. The size, weight and power (SWaP) requirements of ultra-low power RF systems and the Internet of Things has renewed interest in piezoelectric analog signal processing [2–5]. Parallel developments in photonic and optomechanical devices [6–11] and efforts to improve the connectivity and scalability of emerging quantum hardware [12, 13] has led to a fruitful convergence of several strands of research and brought new classes of acoustic structures to the forefront. The valuable library of techniques and intuitions developed for the design of surface acoustic wave devices can only be applied approximately in this new context. Improving our understanding of and ability to control the propagation and transduction of mechanical waves in these thin-film, highly coupled nanostructures is paramount for continued progress in the field.

In this work we study acoustic wave transduction and propagation in thin-film lithium niobate. The piezoelectric coupling coefficient k^2_{eff} and quality factor Q are essential figures of merit across applications. Large k^2_{eff} is necessary for large fractional bandwidth microwave filters and acousto-optic modulators; large field of view acousto-optic deflectors; and small transducers for wavelength-scale waveguides and resonators. Resonators supporting longitudinal and horizontal shear (SH) waves in piezoelectric slabs have been demonstrated with k^2_{eff} as high as 30% and quality factors above 1000 with frequencies between 100 and 500 MHz [2, 3, 14, 15]. These waves which propagate in the plane of the film have also been used to make delay lines and chirped pulse compressors [4, 16]. More recently in thin-film lithium niobate, waves propagating normal to the plane of the film have been used to make resonators supporting a 30 GHz mode with a k^2_{eff} of 1% and a Q over 300. We extend work on the SH and longitudinal waves to higher frequencies for applications in photonic circuits where photon interactions are mediated by phonons with wavelengths on the order of a micron and quantum acoustic systems with qubits operating above 2 GHz. To better understand these transducers, we map out their band structure by varying the interdigitated transducer (IDT) pitch a. We show that SH and longitudinal waves can be efficiently transduced from 1.2 to 3.3 GHz and 2.1 to 5.4 GHz, respectively. We measure a group velocity of 4000 m/s and attenuation constant of 6.0 dB/mm for SH waves at 2 GHz and use these waves to realize a 1.2 mm line with a 300 ns microwave delay.

More broadly, we develop a better understanding of these transducers in terms of their band structure and, by sweeping the number of finger-pairs N, detail the role that resonances play in their response. We numerically study how the conductance spectrum $G(\omega)$ varies going from the low k^2_{eff} regime in which the impulse response model holds to the observed high k^2_{eff} strongly-coupled regime where resonances dominate the response. These resonances decrease the bandwidth and increase the peak conductance of the main lobe, accounting for the large motional admittances exhibited by these small-footprint IDTs.

* sicamor@stanford.edu
† safavi@stanford.edu

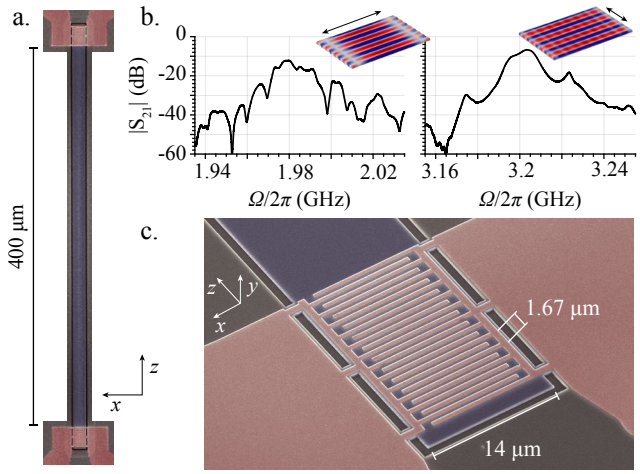

FIG. 1. Straight-finger, uniform pitch and weight aluminum IDT's (red) are deposited on a 250 nm thick $LiNbO_3$ slab (blue) on silicon which is then released. **b.** The IDT's strongly transduce the 2 GHz SH modes (N = 12) and the 3.2 GHz longitudinal response (N = 16).

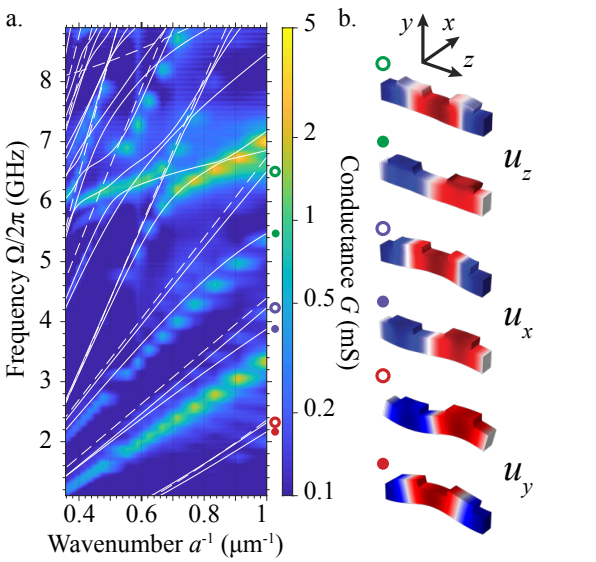

FIG. 2. **a.** The band structure of the IDT is revealed in measurements of the conductance $G(\omega)$ by varying the pitch a. Large peak conductance is measured between 1 and 5 GHz. **b.** A 200 nm cross-section of the displacement u of the modes of the IDT at the X-point of an $a^{-1} = 0.6$ µm^{-1} unit cell are shown at right for the Lamb, horizontal shear, and longitudinal bands. Waves propagate along z. The offset between the bands and the response is analyzed in Section III.

II. S BAND TRANSDUCERS IN SUSPENDED $LiNbO_3$

We start by demonstrating efficient transduction of low-loss SH waves and longitudinal waves from 1.2 to 5.4 GHz before turning our attention to the physics of these high k^2_{eff} IDTs in Section III.

The delay lines studied here are 14 µm wide, 250 nm thick plates of X-cut lithium niobate terminated on each end with aluminum, straight-finger IDTs with a 10 µm finger overlap. The Y crystal axis is parallel and the extraordinary axis (Z) is perpendicular to the direction of propagation [17]. The delay lines are tethered only in the transducer region, with six tethers at each transducer as shown in Figure 1. Devices as long as 1.2 mm were suspended in this manner without collapse. Transducers are etched along the back edge and therefore emit in one direction.

The fabrication methods are adapted from Arrangoiz-Arriola *et al.* [18]. Starting with wafers of 500 nm X-cut $LiNbO_3$ on 500 µm of silicon, chips are diced and ion milled to 250 nm before patterning the tethered membranes by electron beam lithography. These patterns are argon ion-milled into the $LiNbO_3$, the mask is stripped with a piranha clean, and 100 nm of aluminum is evaporated onto a PMMA 950 on PMMA 495 kilodalton lift-off bilayer in which electrodes were defined by e-beam lithography. By correcting for proximity effect, IDTs with pitches ranging from 1 µm (250 nm fingers with 250 nm gaps) to 2.2 µm could be made alongside contact pads with a single mask. After lift-off, the delay lines are released by underetching the silicon with XeF_2 vapor.

The S-parameters of the devices are measured with a vector network analyzer (Rhode & Schwarz ZNB20 VNA) on a probe station with GSG probes (GGB nickel 40A). The probe station is calibrated with a GGB Industries CS-5 substrate to move the reference plane to the tips of the probes. The magnitude of $S_{21}(\omega)$ of 12 and 16 finger-pair IDT's separated by 100 µm is plotted in Figure 1b in which we see responses at 2 and 3.2 GHz corresponding to the horizontal shear (SH) and longitudinal modes. We calculate the single-port admittance $Y(\omega)$ from the $S(\omega)$ matrix [19]. As the conductance $G(\omega) \equiv \text{Re}Y(\omega)$, and the susceptance $\chi(\omega) \equiv \text{Im}Y(\omega)$ are a Hilbert transform pair, it is sufficient to restrict our attention to the conductance and the electrostatic capacitance $C_s \equiv -\lim_{\omega\to 0}\chi_{11}(\omega)/\omega$. For a brief overview of linear response theory and details on conventions used here, see Appendix A. In Figure 5a, measurements of $G(\omega)$ of an $N = 16$, $a = 1.72$ µm transducer for the SH band can be compared to results of a 2D finite element method (FEM) model discussed in detail in Section III.

There are three sets of devices reported here in which the pitch, delay line length, and number of finger-pairs are swept.

The first set of devices consists of 19 IDTs with ten finger-pairs and a pitch a that increases uniformly from 1 to 2.8 µm. The pitch a of the IDT determines the wavelength of the waves it excites. Sweeping the pitch maps out the efficiently transduced IDT bands, apparent in the measured $G(\omega)$ plotted in Figure 2a. The band structure of a free slab (dashed) and the X-point frequencies of the IDT (solid) are computed by the FEM and overlaid on the measured conductance for comparison. The funda-

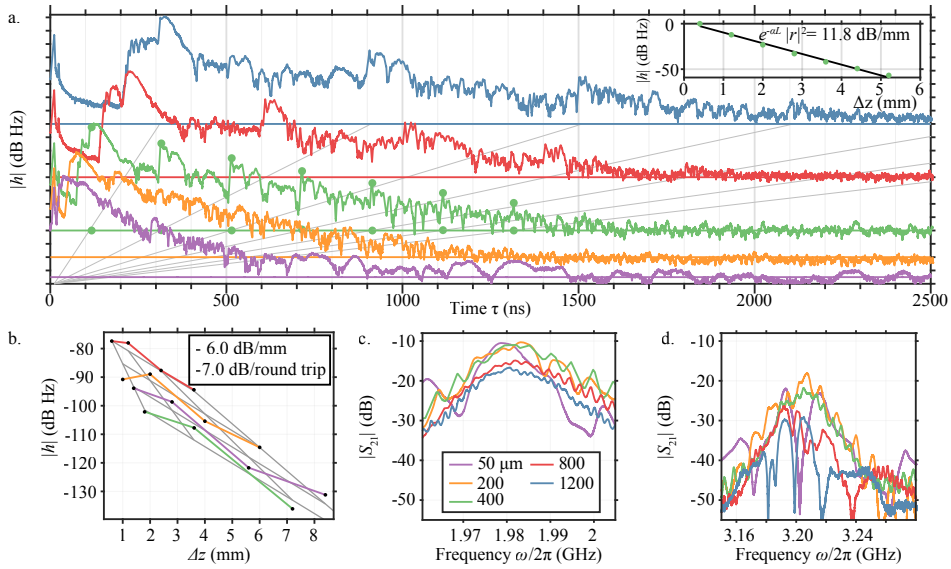

FIG. 3. **a.** The impulse response $h(t)$ is plotted for delay lines of varied length. For the $L = 400$ µm long line (green), the peak height $h(\tau_n)$ of the SH echoes are fit (inset) to infer the round-trip loss $r^2 e^{-\alpha L}$. **b.** Peaks from the longest three lines are fit against the number of round-trips n and total propagation length Δz to find the propagation loss α for the SH waves. In **c.** and **d.** we plot $|S_{21}|$ for the SH and longitudinal modes.

mental horizontal shear and longitudinal modes are seen to vary from 1.2 to 5.4 GHz, spanning the S and entering the C band. We plot the displacement profile of these modes in Figure 2b. In addition, higher order shear modes at 6 GHz are efficiently transduced.

The second set of devices fabricated consists of five delay lines in which two IDTs are separated by a distance that ranges from $L = 100$ µm to 1200 µm. The IDTs are identical with ten finger-pairs spaced by a 1.72 µm pitch. The two-port impulse response $h(\tau)$ of these delay lines is computed by discrete Fourier transform of the $S_{21}(\omega)$, collected in Figure 3, and used to infer the propagation losses. For devices in which the round-trip time exceeds the inverse of the bandwidth of the transducer, distinct echoes $h_\delta(\tau)$ can be identified and used to infer the round-trip loss. The responses shown in Fig. 3a are vertically offset such that constant-velocity features align diagonally. The SH waves propagate with group velocity $v_g = 4.00 \pm 0.03$ km/s. The intersection of the color horiztonal rules with the gray diagonals indicate 1, 2, ... round-trips of the 4000 m/s SH echoes.

If we ignore the effects of dispersion and multimodedness on $h_\delta(\tau)$ and restrict our attention to the SH band, the impulse response takes the form

$$h(\tau) = t^2 e^{-\alpha L/2 - i\omega\tau} \sum_n \left(r^2 e^{-\alpha L}\right)^n h_\delta(\tau - \tau_n) \qquad (1)$$

where the arrival time τ_n is $(1+2n)\,L/v_g$ with group velocity v_g and ω is the center frequency of the transducer. Since the delay line and transducer are multimoded, the squares of the transmission coefficient $|t|^2$ of the IDT (delay line to transmission line) and the reflection coefficient $|r|^2$ (delay line off the IDT) do not in general add to 1 even in the absence of loss. Impedance mismatch decreases $|t|$ and increases $|r|$.

In order to independently infer the propagation loss $e^{-\alpha L}$ and reflection loss $|r|^2$ from measurements, we need to sweep L. A fit to $|h(\tau_n)|$ for the $L = 400$ µm line alone (inset to Figure 3a) yields a round-trip loss $|r|^2 e^{-\alpha L}$ of 11.8 dB for the SH waves at 2 GHz. We independently regress $|t|^2$, $|r|^2$, and α fitting a plane to $|h(\tau_n)|$ against n and nL for delay lines of varied length. In doing so we assume t and r are constant across devices. We find that the power in the 2 GHz SH0 modes drops by $\alpha = 6.0$ dB/mm. This corresponds to a standing-wave resonator instrinsic quality factor of 2300 and an fQ product of 4.6×10^{12}. This α and the $|r|^2$ loss of 7.0 dB is consistent with the round-trip loss of 11.8 dB inset in Figure 3a for which the round-trip length $2L = 800$ µm.

The 14 µm × 1.2 mm delay line has a group delay of 300 ns with an insertion loss of 14.3 dB, 3.4 dB of which comes from impedance mismatch.

The third set of devices fabricated contains 11 delay lines in which N ranges from 4 to 35. The conductances presented in Figure 6 show how the lineshape varies with N and Figure 7 shows the dependence of the main lobe on N. These results reveal the influence of dispersion, reflections, and loss on the IDTs, necessitating a departure from impulse response model as discussed in Section III.

III. DEVIATION FROM THE IMPULSE RESPONSE MODEL

Before accounting for loading by the electrodes, we give a brief overview of the impulse response method of IDT

design [20]. The linear response of the transducer is completely characterized by the static capacitance C_s and the conductance $G(\omega)$. The conductance $G(\omega)$ is the power spectrum of an IDT's impulse response (see Appendix A) which can be related to the IDT geometry by Fourier transform. This forms the basis of the impulse response method of transducer design.

A uniform pitch, uniformly weighted transducer driven by $V = \delta(t)$ emits an Na long rectangular pulse with wavelength a from which, assuming linear dispersion, it follows [20]

$$G(\omega) = G_0 \mathrm{sinc}^2 x. \tag{2}$$

Here $x = N\pi(\omega - \omega_0)/\omega_0$ and $\omega_0 = 2\pi v/a$ where N is the number of finger-pairs, a the pitch, and v is the phase velocity of the mechanical waves. It follows that the full-width-half-maximum γ_{IRM} is

$$\gamma_{\mathrm{IRM}} \approx 0.89 \frac{\omega_0}{N}.$$

The peak conductance is

$$G_0 = 8 f_0 k_{\mathrm{eff}}^2 c_s N^2$$

where k_{eff}^2 is the piezoelectric coupling coefficient and $c_s = C_s/N$ is the capacitance per finger-pair.

The electrode lattice that comprises an IDT electrically and mechanically loads the piezoelectric slab. This changes the dispersion of an IDT and introduces reflections between it and the adjoined slab. In typical surface acoustic wave devices k_{eff}^2 is small and the electrodes are thin relative to the wavelength. These conditions of low electrical and mechanical loading result in reflections on the order of 1% which can be treated as a second-order effect [21, 22].

The devices studied here are outside the range of validity of the impulse model response model, leading to predictions that deviate significantly from measurements and observations. For example, we see that the measured and simulated bandwidth are more than an order of magnitude smaller than would be predicted by the impulse response model (see Figure 7). Moreover, the scaling of the bandwidth with N follows power laws different than N^{-1} (see Appendix B). To understand these effects, we move to a picture that takes into account the presence of a phononic bandgap and localized resonances.

IV. THE ROLE OF RESONANCE AND BANDGAPS

An IDT's electrodes form a lattice that electrically and mechanically loads the slab. This periodic loading couples forward and backward waves with wavelengths close to the pitch of the IDT, giving rise to a bandgap. In principle, a bandgap arises from an arbitrarily small periodic perturbation and can be resolved in an infinitely long, lossless IDT. Finite size and loss obscure the effects of a bandgap. A device with loss rate γ_i will temporally resolve a bandgap of size B when $\gamma_i < B$. A finite-size transducer will spatially resolve the bandgap when B exceeds the inverse transit time which is approximately γ_{IRM}. If the bandgap is resolved both spatially and temporally, we will need to account for its effect to understand the operation of the transducer. We call this regime, in which coupling between forward and backward modes in the IDT cannot be ignored, the *strong coupling* regime.

In order to capture these effects, we model a quasi-2D cross-section of our IDTs using the FEM and scale the results by the finger-overlap, 10 µm, to compare them to measurement. By reducing the problem in this manner we speed up simulations while accounting for both in- and out-of-plane displacement but ignore the transverse mode structure of the IDT and slab. Other methods like the coupling-of-modes (COM) method and Green's function analyses also account for reflections from loading [22].

First we show that for high k_{eff}^2 even when the electrodes are infinitely thin, electrical loading alone causes $G(\omega)$ to deviate significantly from Equation 2. In Figure 4 we scale the piezoelectric tensor d_{ij} by k/k_{LN} between 0 and 1 and calculate $G(\omega)$ for 10 finger-pair, double-sided IDTs with infinitely thin electrodes. As k_{eff}^2 approaches 0, $G(\omega)$ limits to a $\mathrm{sinc}^2 x$ distribution as in Equation 2. As k approaches k_{LN}, the lobes move up in frequency due to piezoelectric stiffening and the high frequency sidelobes shift away from the main lobe to form a large, flat pedestal. In measurements in Figure 5a and Figure 6b, standing waves in the delay line form Fabry-Pérot peaks in the pedestal with a free spectral range of 20 MHz.

In Figure 4b we plot the the simulated linewidth (full-width-half-maximum γ, solid black) along with linewidth of the impulse response model(γ_{IRM}, dashed), derived from the transit time, and the intrinsic damping rate (γ_i, dashed) which bound γ above and below, respectively. The bandgap B increases with k/k_{LN}, intersecting γ_{IRM} at $k = 0.74 k_{\mathrm{LN}}$. Above this point, the IDT is strongly coupled for $N = 10$ finger pairs. We note that above $k = 0.57 k_{\mathrm{LN}}$ the bandgap is well-resolved, exceeding the transducer linewidth γ.

The asymmetry of the lineshape in Figure 4 can be understood in terms of the band structure of the electrode lattice in the high k_{eff}^2 limit. In Figure 5b, we plot the bands for infinitely thin (blue) and 100 nm thick electrodes (black). The avoided crossing at the X-point $K = 2\pi/a$ suppresses the response $G(\omega)$ between the band edges forming the pedestal of Figure 4. For ease of comparison we overlay the X-point frequencies over the domain of k/k_{LN} in Figure 4 (dashed). For the IDTs measured, the 100 nm thick aluminum electrodes also have a significant elastic effect, shifting up and reducing the size of the bandgap.

For a fixed frequency, waves propagating in the electrode lattice have a different K, group velocity v_g, and

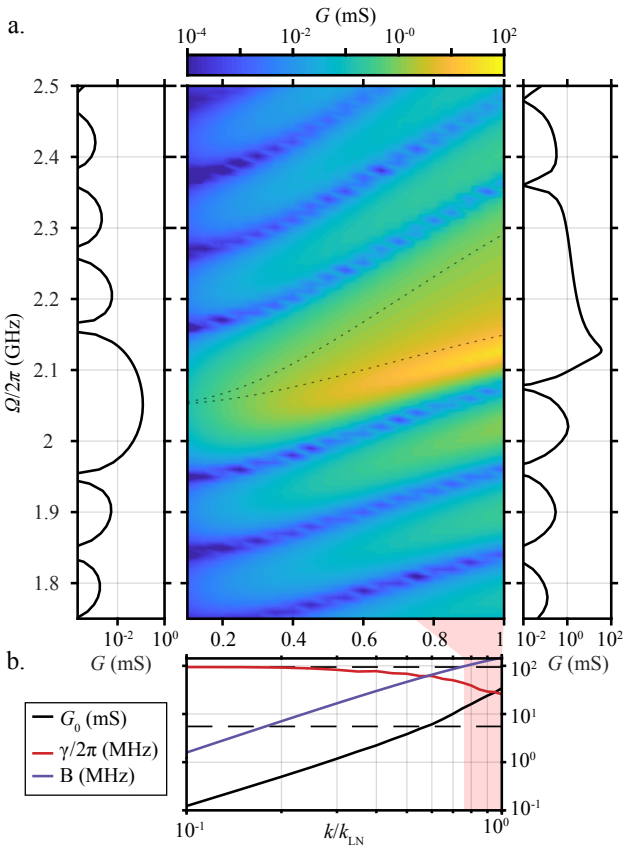

FIG. 4. We scale the coefficients of the piezoelectric tensor by k/k_{LN} for 10 finger-pair, double-sided IDTs with infinitely thin electrodes to isolate the effect electrical loading has on the lineshape of $G(\omega)$. The conductance $G(\omega)$ limits smoothly between the $\mathrm{sinc}^2 x$ impulse response regime and the high k^2_{eff} resonant regime. The bandgap is overlaid, coinciding with the lobe-free pedestal that forms with high k. The linewidth and peak conductance of the main lobe are plotted in **b.**. The linewidth γ is bounded above by the impulse response model and below by intrinsic losses (both dashed). Strong coupling occurs when the splitting B exceeds γ_{IRM} which happens for $N = 10$ at $k/k_{\mathrm{LN}} > 0.74$.

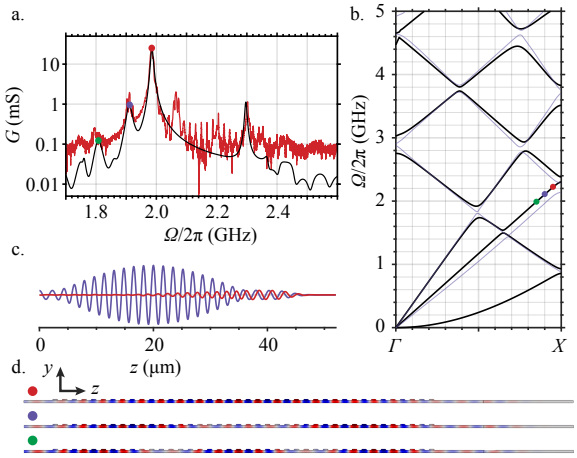

FIG. 5. **a.** Measurements (red) of $G(\omega)$ are compared to lossless FEM models (black) with loss $Q_{\mathrm{i}} = 300$ and $k/k_{\mathrm{LN}} = 0.67$. The lobes marked with a red, blue, and green point correspond to those on the SH0 band of a unit cell of the IDT in **b.** and the FEM solutions in **d.**. In **d.** we see the lobes can be identified by the number of nodes in the envelope. The quadratures of the displacement u_x of the main lobe (red point) along the bottom surface is plotted in **c.**. The 2.3 GHz feature in **a.** originates from a resonance near the back edge.

mode shape than those of the free slab. Reflections at the interface from this discontinuity result in standing waves within the IDT as shown in Figure 5c. In Figure 5d we plot the fundamental, first-excited, and second-excited resonances of the negative mass band (normal group velocity dispersion $\partial_\omega v_{\mathrm{g}} < 0$) which correspond to the main lobe and first two low frequency sidelobes. Likewise resonances originating from the positive mass band correspond to the high frequency sidelobes in Figures 4 and 6. In varying k/k_{LN} between 0 and 1 we see a smooth transition from the lobes of the impulse response which come from the K distribution of the envelope to the resonant structure of the IDT.

The strain S_{xz} of the negative and positive mass SH modes is localized in the gaps and under the electrodes, respectively, as seen in Figure 2b. These modes sample different components of the applied electric field, E_z and E_y, and therefore different components of the piezoelectric tensor, d_{YYZ} ($d_{24} = d_{15}$ in Voigt notation; here capitals denote crystal axes) and $d_{\mathrm{XYZ}} \equiv d_{14} = 0$ pN/C, respectively. This contributes to the asymmetry of $G(\omega)$ and accounts for the relatively weak positive mass response in the simulated and measured conductance in Figure 6. Changing d_{ij} by, for example, rotating the crystal changes the relative strength of these responses.

The momentum of the fundamental resonance is broadened by the spread in envelope momentum $K_{\mathrm{e}} = 2\pi/Na$. As N increases and K_{e} approaches 0, the center frequency of the main lobe shifts toward the band edge, increasing for the negative mass modes and decreasing for the positive mass modes. The sidelobes are similarly offset from the band edge by K_{e} resulting in the N-dependent lobe shifts in Figure 5a and Figure 6.

Loading affects not only the lineshape but also the shape of the lobes of $G(\omega)$. Dispersion and reflections narrow γ and increase G_0 of the main lobe relative to Equation 2. Consider the SH response of a 16 finger-pair transducer. A 10 μm wide IDT has a capacitance of 45 fF computed by the FEM. Assuming $k^2_{\mathrm{eff}} = 13\%$, a γ of $2\pi \times 110$ MHz and G_0 of 1.5 mS follows from Equation 2. Instead we measure $2\pi \times 9.6$ MHz and 25 mS, underscoring the necessity of accounting for loading.

In Figure 7 we plot G_0 and γ extracted from Figure 6 by fitting Lorentzians to $G(\omega)$ for simulations (blue points) and measurements (black points) and compare them to Equation 2 (red). We simulate the system, accounting for electrical and mechanical loading, but ne-

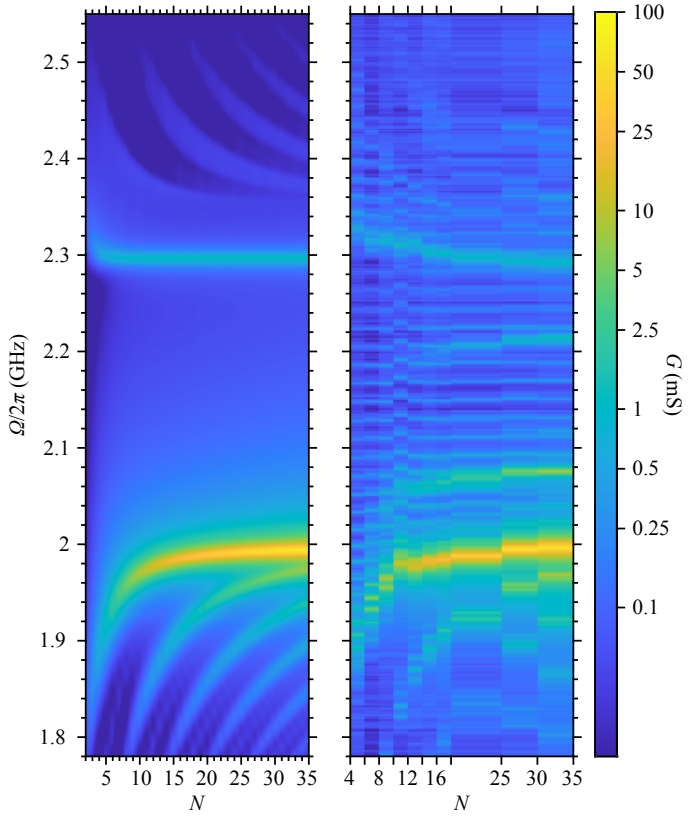

FIG. 6. The simulated and measured conductance $G(\omega)$ is plotted against the number of finger-pairs N for the SH mode. In these plots we can identify the bandgap beset below by the strongly transduced negative mass band resonances which shift up with N and above by the weakly transduced positive mass band resonances which shift down with N. Resonances along the etched back edge of the IDT appear as often strongly transduced peaks that are nearly independent of N.

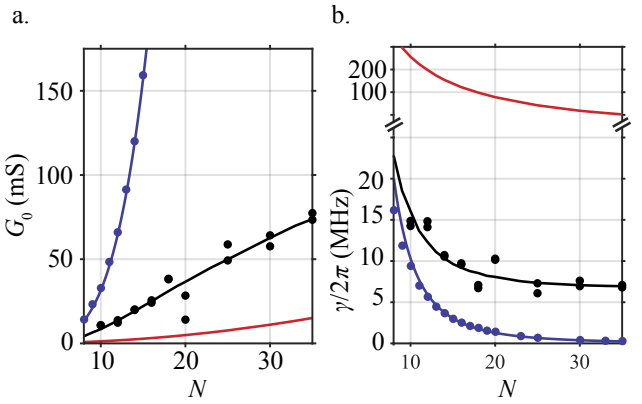

FIG. 7. Lorentzians are fit to the measured and computed conductance $G(\omega)$ of Figure 6 and their peak height G_0 and FWHM γ are plotted in **a** and **b**. Simulations without loss are plotted in blue. By adding intrinsic damping γ_i and reducing d_{ij} by a factor of 0.67, the response becomes that of the black curves. Measured responses are plotted as black points. The red curves are predictions from the impulse response model.

glecting losses. We observe an approximate N^{-3} scaling of the bandwidth γ, as opposed to the N^{-1} found in Equation 2 and equivalent circuit models [23]. As shown in the Appendix, we vary the level of electrical and mechanical loading to find a family of scaling laws between N^{-1} and N^{-3}. In the highly coupled N^{-3} limit, the stronger suppression of the bandwidth with increasing N can be understood using a resonant Fabry-Pérot model of the IDT. Waves traveling within the IDT are reflected from the IDT/slab interface with a reflection coefficient r approximately determined by a group velocity mismatch

$$r = \frac{v - v_g}{v + v_g},$$

where v_g and v are the group velocities in the IDT and slab, respectively. These reflections lead to a standing wave inside the IDT with a linewidth

$$\gamma = \frac{2v_g}{Na}\frac{1-r^2}{2r} \underset{r\to 1}{\rightarrow} \frac{2v_g}{Na}(1-r) = \frac{4v_g^2}{Nav}.$$

We assume that the fundamental resonance of the IDT is sufficiently close to the X-point for the dispersion to be nearly quadratic, *i.e.*, $v_g = \beta K_e$ for some constant β. The spread in the envelope momentum $K_e = 2\pi/Na$ for the fundamental standing wave is inversely proportional to N. This leads to an expression for the linewidth

$$\gamma = \frac{16\pi^2\beta^2}{va^3}\frac{1}{N^3},$$

matching the simulated power law. In addition to the original factor of N^{-1} in Equation 2 from the length of the transducer, the group velocity dispersion and the variation in the IDT-slab reflection coefficient each contribute another factor of N^{-1}. The conductance G_0 is seen to scale approximately as N^4 in the same lossless simulations.

It is clear from Figure 7a that the measured bandwidth γ stops narrowing at large N and approaches 7 MHz in the high N limit. This intrinsic linewidth γ_i corresponds to a Q of approximately 300, significantly lower than the Q of 2300 corresponding to the 6.0 dB/mm propagation losses measured for the 4000 m/s SH waves. Incorporating this loss rate into our FEM models by adding a uniform material loss tangent across the domain and reducing d_{ij} by $k/k_{LN} = 0.67$ yields the black curves in Figure 7a and b in close agreement with measurements. The same material loss and reduction in k are also used in the simulations of Figure 6. We attribute these discrepancies to mechanical losses in the aluminum electrodes and discrepancies between the material properties in thin-film and bulk $LiNbO_3$, and are investigating techniques for improving the films' properties.

We note here that G_0 increases at the expense of γ such that $G_0\gamma$ remains proportional to N. This is a more general statement that holds regardless of the exact de-

pendence of γ and G_0 on N, and is a direct consequence of the extensivity of the net conductance $\int \mathrm{d}\omega G(\omega)$. As we will report in a future manuscript, the net conductance of a narrowband transducer can be directly related to k^2_{eff}

$$k^2_{\mathrm{eff}} = \frac{\int \mathrm{d}\omega G(\omega)}{16\pi C_{\mathrm{s}} f_0^2}$$

from which we find a k^2_{eff} of 10% (area in the main lobe). By comparing the measured static capacitance C_{s} to simulations, we attribute a factor of 1.3 reduction in k^2_{eff} to 22 pF of feedthrough capacitance [24]. For $k = k_{\mathrm{LN}}$ the simulated k^2_{eff} is 30%. The discrepancy between the simulated 30% and measured 13% coincides with our choice of k/k_{LN} in Figures 6a and 7.

V. CONCLUSION

The mechanical confinement and large k^2_{eff} of piezoelectric devices in suspended $LiNbO_3$ slabs makes the platform an attractive candidate for a host of GHz-frequency applications. Here we demonstrated efficient transduction of SH and longitudinal waves from 1.2 to 5.4 GHz by transducers with small footprints, 14×17 µm. At 2 GHz the SH waves are strongly-coupled to the IDTs with k^2_{eff} reaching 13% (after correcting for feedthrough capacitance). Propagation losses for the SH waves are measured, 6.0 dB/mm, and the waves are used to make a 1.2 mm with a 300 ns delay.

In this high k^2_{eff} regime even in the absence of mechanical loading, electrical loading modifies the dispersion in the IDT introducing a bandgap, reflections, and resonance. We confirmed this by studying the way the lineshape and lobe shape of the conductance $G(\omega)$ vary with the number of finger pairs N of the IDT. The lineshape exhibits a large lobe-free pedestal in the bandgap encased by positive and negative mass band resonances which shift toward the band edge as N is increased. Furthermore the main lobe linewidth is more strongly suppressed with increasing N than in the impulse response regime. This accounts for the larger-than-expected motional admittance of these small-footprint IDTs.

For narrowband applications like the transduction of nanoresonators and waveguides for quantum devices, cavity optomechanics, or RF filters, the enhancement of the peak conductance that comes with resonance is tolerable and perhaps even desirable. Small-footprint IDTs make it easier to couple to small mechanical devices, match them to 50 Ω, and achieve large coupling. But for some wideband applications in optomechanics and RF signal processing – applications with bandwidth requirements that drive the pursuit of high k^2_{eff} transducers – reflections consequent to high k^2_{eff} may pose a challenging constraint on device architecture and IDT design. In addition to demonstrating small, high k^2_{eff} transducers, our work delineates the regimes in which these effects are at play.

VI. ACKNOWLEDGEMENTS

C.J.S. and A.S.N. would like to thank John Larson, Victor Plessky, Leonhard Reindl, Songbin Gong, Gabriel Vidal Álvarez, and Don and Svetlana Malocha for valuable discussions. This work was funded by the National Science Foundation through ECCS-1808100 and by the U. S. Air Force Office of Scientific Research through a MURI grant (Grant No. FA9550-17-1-0002). Part of this work was performed at the Stanford Nano Shared Facilities (SNSF) and Stanford Nanofabrication Facility (SNF) which are supported by the National Science Foundation under award ECCS-1542152. A.S.N. acknowledges the support of a David and Lucile Packard Fellowship. A.Y.C. is supported by the Stanford Graduate Fellowship program.

[1] D. Morgan, in *Proceedings of the 1998 IEEE International Frequency Control Symposium (Cat. No.98CH36165)* (IEEE, 2002) pp. 439–460.
[2] R. H. Olsson, K. Hattar, S. J. Homeijer, M. Wiwi, M. Eichenfield, D. W. Branch, M. S. Baker, J. Nguyen, B. Clark, T. Bauer, and T. A. Friedmann, Sensors and Actuators A: Physical **209**, 183 (2014).
[3] Y. H. Song, R. Lu, and S. Gong, IEEE Transactions on Electron Devices **63**, 2066 (2016).
[4] T. Manzaneque, R. Lu, Y. Yang, and S. Gong, Journal of Microelectromechanical Systems **26**, 1204 (2017).
[5] S. Gong, Y.-H. Song, T. Manzaneque, R. Lu, Y. Yang, and A. Kourani, in *2017 IEEE 60th International Midwest Symposium on Circuits and Systems (MWSCAS)* (IEEE, 2017) pp. 45–48.
[6] C. J. Sarabalis, R. Van Laer, and A. H. Safavi-Naeini, Optics Express **26**, 22075 (2018).
[7] A. H. Safavi-Naeini, D. Van Thourhout, R. Baets, and R. Van Laer, Optica **6**, 213 (2019).
[8] M. Mahmoud, A. Mahmoud, L. Cai, M. Khan, T. Mukherjee, J. Bain, and G. Piazza, Optics Express **26**, 25060 (2018).
[9] E. A. Kittlaus, H. Shin, and P. T. Rakich, Nature Photonics **10**, 463 (2016).
[10] D. B. Sohn, S. Kim, and G. Bahl, in *2018 IEEE Photonics Conference (IPC)* (IEEE, 2018) pp. 1–2.
[11] S. A. Tadesse and M. Li, Nature Communications **5**, 5402 (2014).
[12] K. J. Satzinger, Y. P. Zhong, H. S. Chang, G. A. Peairs, A. Bienfait, M. H. Chou, A. Y. Cleland, C. R. Conner, Dumur, J. Grebel, I. Gutierrez, B. H. November, R. G. Povey, S. J. Whiteley, D. D. Awschalom, D. I. Schuster, and A. N. Cleland, Nature **563**, 661 (2018).
[13] M. Pechal, P. Arrangoiz-Arriola, and A. H. Safavi-Naeini, Quantum Science and Technology **4**, 015006

(2018).
[14] I. Kuznetsova, B. Zaitsev, S. Joshi, and I. Borodina, IEEE Transactions on Ultrasonics, Ferroelectrics and Frequency Control **48**, 322 (2001).
[15] F. V. Pop, A. S. Kochhar, G. Vidal-Alvarez, and G. Piazza, in *2017 IEEE 30th International Conference on Micro Electro Mechanical Systems (MEMS)* (IEEE, 2017) pp. 966–969.
[16] G. Vidal-Alvarez, A. Kochhar, and G. Piazza, in *2017 IEEE International Ultrasonics Symposium (IUS)* (IEEE, 2017) pp. 1–4.
[17] R. S. Weis and T. K. Gaylord, Applied Physics A Solids and Surfaces **37**, 191 (1985).
[18] P. Arrangoiz-Arriola, E. A. Wollack, M. Pechal, J. D. Witmer, J. T. Hill, and A. H. Safavi-Naeini, Physical Review X **8**, 031007 (2018).
[19] D. M. Pozar, *Microwave engineering*, 3rd ed. (John Wiley & Sons, Inc., 2009).
[20] C. Hartmann, D. Bell, and R. Rosenfeld, IEEE Transactions on Microwave Theory and Techniques **21**, 162 (1973).
[21] W. Jones, C. Hartman, and T. Sturdivant, IEEE Transactions on Sonics and Ultrasonics **19**, 368 (1972).
[22] D. P. Morgan, *Surface acoustic wave filters: With applications to electronic communications and signal processing* (Academic Press, 2010).
[23] W. Smith, H. Gerard, J. Collins, T. Reeder, and H. Shaw, IEEE Transactions on Microwave Theory and Techniques **17**, 856 (1969).
[24] S. Gong and G. Piazza, IEEE Transactions on Microwave Theory and Techniques **61**, 403 (2013).

Appendix A: Linear response of a transducer

Consider an N finger-pair transducer with anode-to-anode spacing, or *pitch*, a and uniform finger overlap, or *weighting*, w. The transducer is a linear time-invariant system and is thus described within the context of linear response theory. Applying a voltage $V(t')$ across the device draws a current $I(t)$ related to V by the impulse response function $Y(t-t')$

$$I(t) = \int_{-\infty}^{\infty} \mathrm{d}t' Y(t-t') V(t').$$

A δ-distributed drive $V(t') = \delta(t')$ generates a current $Y(t)$.

For time-invariant systems where the impulse response depends only on the difference $t-t'$, it takes a simple form in the frequency domain

$$I(\omega) = Y(\omega) V(\omega) \tag{A1}$$

where

$$V(t) = \frac{1}{2\pi} \int_{-\infty}^{\infty} \mathrm{d}\omega V(\omega) e^{-i\omega t}$$

and similarly for the current I. The impulse response $Y(t)$ and circuit admittance $Y(\omega)$ are related by a Fourier transform. Since the voltage $V(t)$ is a real-valued function, the complex amplitude $V(-\omega)$ is equal to $V^*(\omega)$, similarly for $I(\omega)$, and therefore $Y(\omega)$.

For a single port device such as an IDT terminating a transmission line, measurements of reflections encoded in the scattering parameter $S_{11}(\omega)$ can be used to compute the admittance

$$Y(\omega) = Y_0 \frac{1 - S_{11}(\omega)}{1 + S_{11}(\omega)}$$

where Y_0 is the admittance of the transmission line, often 20 mS. For a two-port device, the linear response can be captured by an admittance matrix with components Y_{ij} which can be computed from elements of the scattering matrix S_{ij} [19]. The scattering matrix can be measured using a vector network analyzer from which one can compute the impulse response

$$Y(t) = \frac{1}{2\pi} \int_{-\infty}^{\infty} \mathrm{d}\omega Y(\omega) e^{-i\omega t}$$

with units of Hz/Ω. A lot of the information about the response of a system is encoded in the phase of S_{11} which often has a simpler structure and interpretation in the time-domain as shown in Section II.

The real part of the admittance, the *conductance* $G(\omega)$, is related directly to the time-averaged power dissipated by a system. The power dissipated by a system $\mathcal{P}$ is the product of the voltage and current; therefore the spectrum of the dissipated power is the convolution of $V(\omega)$ and $I(\omega)$. Averaging in time extracts the DC component of the power $\mathcal{P}_0$, reducing the convolution to the cross product $V(\omega) I(-\omega) + V(-\omega) I(\omega)$ integrated over positive ω. Thus we find

$$\mathcal{P}_0 = \int_{-\infty}^{\infty} \mathrm{d}\omega G(\omega) |V(\omega)|^2 \tag{A2}$$

which is a weighted average of the power spectral density of V. Causality constrains the linear response such that the conductance and the imaginary part of $Y(\omega)$, the *susceptance*, are a Hilbert transform pair and therefore not independent quantities. Computing $G(\omega)$ and the electrostatic capacitance C_s is a complete description of the linear response.

If we ignore material losses, resistive losses, and microwave radiation, the power dissipated by the IDT radiates away as mechanical waves in the lithium niobate. Because we can relate the power-dissipated to the radiated power, we can directly compute the conductance $G(\omega)$ from the power-spectrum of the mechanical fields impulse-response. This forms the basis of the impulse response method [20].

Appendix B: Dependence of the linewidth and peak conductance on mechanical and electrical loading

It's reasonable to suspect that the resonance and reflections arise predominately from the mechanical, not

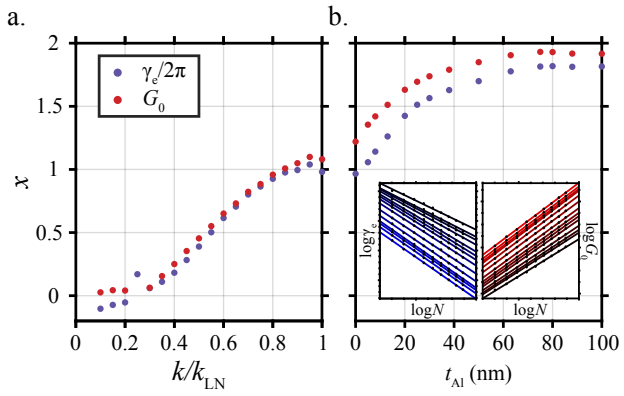

FIG. 8. By computing $G(\omega)$ and fitting the main lobe to a Lorentzian for IDTs with N ranging from 10 to 18, we can extract the exponent x with which the peak conductance G_0 and bandwidth γ scales. Sweeping k^2_{eff} (**a**) and the electrode thickness t_{Al} (**b**) reveals their independent contributions to the resonant behavior of the IDTs. When $t_{\text{Al}} = 0$ the power-laws strongly deviate from the impulse response model $x = 0$ due to the large k^2_{eff} of these IDTs. Power-law fits to the t_{Al} sweep are inset to **b.**.

electrical, loading by the electrodes. The electrodes are 100 nm thick, a significant fraction of the 250 nm $LiNbO_3$ slab. If this was the case, as the electrode thickness approaches 0, the peak conductance G_0 would scale as N^2 and the FWHM γ as N^{-1} as in Equation 2 of the impulse response model.

To investigate this limit, we compute the conductance $G(\omega)$ for IDTs between 10 and 18 finger-pairs, scaling the piezoelectric tensor **d** by k/k_{LN} between 0.1 to 1 and the electrode thickness from 0 to 100 nm. Lorentzians are fit to $G(\omega)$ and the resulting parameters are fit against N on a log-log plot. The exponents x are plotted in the form

$$G_0 \propto N^{2+x} \tag{B1}$$

$$\gamma \propto N^{-1-x}. \tag{B2}$$

The N^{-3} high t_{Al} and k^2_{eff} limit of γ is given context in Section III. Even when $t_{\text{Al}} = 0$ nm, γ and G_0 deviate from the power-law scaling of Equation 2.

In Figure 8, it is clear that the exponent x fit from G_0 matches that of γ such that $G_0\gamma$ remains proportional to N. This shows the trade-off between peak conductance and bandwidth. The peak conductance is enhanced by the quality factor of the IDT (Appendix C). Material losses decrease Q and therefore G_0. These results are consequences of the net conductance's extensivity and insensitivity to loss on which we will report in a separate manuscript.

Appendix C: Computing γ

The bandwidth of a lossless IDT is equal to γ_e, the rate at which energy leaks out of the transducer. The quality factor is the ratio of the frequency and bandwidth, or equivalently, given by the product of the group delay $\tau_g = \partial\phi_{12}/\partial\omega$ and frequency:

$$Q = \frac{\omega_0}{\gamma_e} = \frac{\tau_g \omega_0}{2} \tag{C1}$$

$$= -\frac{1}{2}\max_{\omega}\left[\omega\frac{\partial\phi_{21}}{\partial\omega}\right] \tag{C2}$$

where ϕ_{21} is the phase difference between the drive $V(\omega)$ and the emitted mechanical wave u_x. Reflections increase the delay and therefore the Q of the IDT. For these highly resonant IDTs, Q can also be inferred from the FWHM of a Lorentzian fit to $G(\omega)$ or from the eigenvalue λ of the resonance

$$Q = \frac{\text{Re}\lambda}{2\text{Im}\lambda}.$$